JPET Fast Forward. Published on April 1, 2019 as DOI: 10.1124/jpet.119.257022
This article has not been copyedited and formatted. The final version may differ from this version.

JPET# 257022

In Vivo Imaging of Small Molecular Weight Peptides for Targeted Renal Drug Delivery: A Study in Normal and Polycystic Kidney Diseased Mice

Steve Lenhard[1*], Allen McAlexander[4*], Anthony Virtue[2*], William Fieles[3], Tina Skedzielewski[1], Mary Rambo[1], Han Trinh[3], Shih-Hsun Cheng[1], Hyundae Hong[1], Albert Isidro-Llobet[5], Alan Nadin[5], Robert Geske[3], Jean-Louis Klein[3], Dennis Lee[4], Beat M Jucker[1], Erding Hu[2].

*authors contributed equally to the publication.

Affiliations:
[1]Bioimaging, [2]Renal Discovery Group, Future Pipeline Discovery, [3]Experimental Cell and Tissue Biology, Target and Pathway Validation, [4]Drug Delivery, [5]Drug Design and Selection, GlaxoSmithKline plc, 1250 South Collegeville Road, Collegeville, PA 19426

Please send correspondence to:

Erding Hu

Mail Stop: UP1W-1210

GlaxoSmithKline plc (GSK)

1250 South Collegeville Road,

Collegeville, PA 19426,

USA

Tel: 1-484-923-3503

Fax: 1-610-917-5670

Email: Erding.Hu@gsk.com

JPET# 257022

Running Title Page

Running Title: Renal targeting in normal and polycystic kidney disease mice

Corresponding author:

Erding Hu

Mail Stop: UP1W-1210

GlaxoSmithKline plc (GSK)

1250 South Collegeville road,

Collegeville, PA 19426,

USA

Tel: 1-484-923-3503

Fax: 1-610-917-5670

Email: Erding.Hu@gsk.com

Word count:

Text pages: 28

Tables: 1

Figures: 6

References: 26

Abstract word count: 250

Introduction word count: 505

Discussion word count: 1444

Abbreviations:

Nonstandard abbreviations (alphabetical order):

ADPKD:	Autosomal dominant polycystic kidney disease
AQP1:	Aquaporin-1
ccRCC:	clear cell renal cell carcinoma
chRCC:	chromophobe renal cell carcinoma
DIPEA:	*N,N*-Diisopropylethylamine
DMF:	*N,N*-Dimethylformamide
ESRD:	End stage renal disease
Fmoc:	9-Fluorenylmethoxycarbonyl
FMT:	Fluorescence molecular tomography
HPLC:	High performance liquid chromatography
IHC:	Immunohistochemistry
LCMS:	liquid chromatography-mass spectrometry
MRI:	Magnetic resonance imaging
NIR:	Near Infrared
NMP:	*N*-Methyl-2-pyrrolidone
pRCC:	papillary renal cell carcinoma
RCC:	renal cell carcinoma
SPPS:	solid-phase peptide synthesis
TFA:	trifluoroacetic acid
TMA:	tumor tissue microarray
VT 680:	VivoTag 680 dye

Recommended section: Gastrointestinal, Hepatic, Pulmonary and Renal

Abstract

Autosomal Dominant Polycystic Kidney Disease (ADPKD) is a leading monogenetic cause of end stage renal disease (ESRD) with limited therapeutic repertoire. A targeted drug delivery strategy that directs a small molecule to renal niches around cysts could increase safety margins of agents that slow the progression of ADPKD but are poorly tolerated due to extra-renal toxicity. Herein, we determined whether previously characterized lysine- and glutamic acid-based, megalin-binding peptides can achieve renal specific localization in the Juvenile Cystic Kidney (JCK) mouse model of polycystic kidney disease and if the distribution is altered compared to control mice. We performed *in vivo* optical and MRI imaging studies using peptides conjugated to the VivoTag 680 dye and demonstrated that megalin-interacting peptides distributed almost exclusively to the kidney cortex in both normal and JCK mice. Confocal analysis demonstrated that the peptide-dye conjugate distribution overlapped with megalin-positive renal proximal tubules. However, in the JCK mouse, the epithelium of renal cysts did not retain expression of the proximal tubule markers aquaporin 1 and megalin, and therefore these cysts did not retain peptide-dye conjugates. Furthermore, human kidney tumor tissues were evaluated by immunohistochemistry and revealed significant megalin expression in tissues from renal cell carcinoma patients, raising the possibility that these tumors could be treated using this drug delivery strategy. Taken together, our data suggest that linking a small molecule drug to these carrier peptides could represent a promising opportunity to develop a new platform for renal enrichment and targeting in the treatment of ADPKD and certain renal carcinomas.

Introduction

Autosomal Dominant Polycystic Kidney Disease (ADPKD) is the most common inherited cause of kidney disease, afflicting greater than 12 million people worldwide (Chapman et al., 2015). The development and uncontrolled growth of fluid filled cysts within both kidneys leads to disorganization of the highly structured organ. As a result, kidney function becomes compromised, leading to kidney failure in 50% of patients within the fifth decade of life. An attractive therapeutic approach for ADPKD is the repurposing of already approved antiproliferative agents typically utilized in cancer. In fact, a wide range of these agents have been shown to be efficacious in preclinical models of ADPKD (Muller and Benzing, 2018). However, these therapeutics have failed to demonstrate clinical benefits primarily due to poor tolerability and/or dose-limiting, mechanism-based extra-renal toxicity (Weimbs et al., 2018). The ability to selectively target the kidneys for drug delivery would minimize exposure in other tissues, thus enabling the development of novel and more efficacious drugs or the repurposing of pre-approved antiproliferative therapeutics by reducing the extra-renal side effects associated with these agents.

One strategy to facilitate renal drug targeting is the conjugation of therapeutics to lysine (K)- and glutamic acid (E) containing peptides. Wischnjow et al demonstrated that a short KE containing peptide is capable of renal targeting in normal mice via megalin-mediated endocytosis (Wischnjow et al., 2016). It is well established that small molecular weight peptides and low molecular weight proteins are reabsorbed from the filtrate via receptors on the apical surface of proximal tubule cells by the integral membrane protein megalin (Christensen and Birn, 2002). Megalin is a central driver of filtered peptide/protein reabsorption into the proximal tubule epitheliumby facilitataing their endocytosis via a series of downstream effector proteins (De et al., 2014). The importance of megalin in driving reabsorption of peptides from the filtrate is underscored by the albuminuria and low molecular weight proteinuria in megalin knockout mice (Leheste et al., 1999). Given megalin's vital role in peptide reabsorption, megalin-binding peptides may serve as versatile scaffolds to enable selective renal targeting. Indeed, a series of lysine and glutamic acid-containing small peptides have been shown to selectively deliver small molecules to the renal cortex in rat and multiple

JPET Fast Forward. Published on April 1, 2019 as DOI: 10.1124/jpet.119.257022
This article has not been copyedited and formatted. The final version may differ from this version.

mouse strains (Wischnjow et al., 2016). The genetic knock out of megalin reduced renal retention of these labeled peptides confirming the role of megalin in the reabsorption of these peptides from the filtrate.

In the present study, we employed a novel imaging modality to evaluate the kidney distribution of two KE containing small peptides in both control mice and a well-established model of ADPKD, Juvenile Cystic Kidney (JCK) mice. An optical and MRI co-registration analysis was carried out to quantify the kidney signal distribution followed by high resolution confocal imaging analysis to determine whether small peptide sequences can target a Near Infra-red (NIR) dye to specific regions/cells of the kidney where cysts typically form. Finally, we examined the possible utility of these peptides in other kidney diseases by assessing the presence of megalin within human kidney neoplasms such as renal cell carcinoma (RCC).

Methods:

*Synthesis of Targeting Peptides (*Aminohexanoic-(KKEEE)$_n$K-amide) *and VivoTag 680 XL dye conjugation*:

VivoTag® 680 XL (PerkinElmer, Waltham, MA) is a near infrared dye ideally suited for *in vivo* imaging. However, the synthesis of N-terminal labelled peptides can be challenging due to the high cost of the VivoTag 680 XL carboxylic acid building block and the use of a large excess of reagent typical of Solid-phase peptide synthesis (SPPS). Instead, an inverse approach was applied in which 0.3-0.5 eq of VivoTag 680 dye was used and the corresponding tagged and untagged peptides were easily separated by semipreparative high-performance liquid chromatography Gilson PLC 2020.

Resin-bound untagged peptides were obtained by the Fmoc/^{t}Bu solid-phase peptide synthesis (SPPS) strategy on a Rink Amide AM polystyrene resin (Novabiochem-EMD Bio, La Jolla, CA, 0.05 mmol, 0.69 mmol/g) using the CEM Liberty 1 microwave peptide synthesizer. Each amino acid was coupled once using the following conditions: Fmoc-amino acid (Merck KGaA-Millipore, Burlington MA, 2.5 mL, 10 equiv., 0.2M in DMF), HCTU (Chem-Impex, Wood Dale, IL, 1.0 mL, 10 equiv., 0.5M in DMF), DIPEA (Aldrich, St. Louis, MO, 1 mL, 10 equiv, 1M in NMP) at 75 ^{o}C for 10 minutes. Fmoc group removals were performed using 20% piperidine in DMF. Fmoc-Aminohexanoic acid was coupled manually using HATU as opposed to HCTU.

Aliquots of resin were then labelled with VivoTag 680 XL Fluorochrome (0.3-0.5 eq) in DMF using PyBOP (Fluorchem, Derbyshire, UK), HOAt (Fluorchem) and DIPEA as coupling reagents for 90 min at room temperature. Cleavage from the solid-support and final deprotection was performed with TFA-H2O (95:5) for 90 min at room temperature. The solvent was then removed under reduced pressure and the resulting crude peptides were purified by semipreparative HPLC (solvent A= 0.1% trifluoroacetic acid in water, solvent B= 0.1%TFA/90% acetonitrile/10% water) and freeze dried. The desired labelled peptides were characterized by LCMS (>90% purity):

GSK601A (KKEEE)$_2$K: 8.3 mg (41% yield)

GSK599A $(KKEEE)_3K$: 6.7 mg (54% yield)

In vivo Optical Imaging:

All mouse studies were approved by GlaxoSmithKline's Institutional Animal Care and Use Committee (IACUC). Eight-week-old female SKH1 Hairless mice (Charles River Labs, Horsham, PA) were used as control mice and 12 week old male Juvenile Cystic Kidney (JCK) mice (Crown BioScience, San Diego, CA) were used for as disease model mice. Mice were anesthetized with 2% isoflurane and 1 L/min medical grade air for *in vivo* imaging. Mice were injected via tail vein with either the control dye, VivoTag 680, GSK601A or GSK599A (Fig. 1A). Each mouse received 200 μg of peptide-dye conjugate which was injected into the tail vein in 100 μL of PBS. *In vivo* optical imaging (IVIS Spectrum-CT, Perkin Elmer, Waltham, MA) was performed at 15 minutes, 1 hour, and 4 hours post injection (Fig. 1B). Following four-hour post-dose *in vivo* optical imaging, mice were euthanized, and brain, heart, liver, spleen and kidneys were excised for ex vivo optical imaging in the IVIS Spectrum-CT and Licor Odyssey imaging systems (LI-COR Inc., Lincoln, NE). Upon completion of *ex vivo* imaging, the organs were placed in OCT and frozen at -80°C for preservation for confocal imaging and analysis.

In vivo/Ex vivo Imaging

In vivo and *ex vivo* optical imaging were performed using a 2D IVIS-Spectrum-CT system. After a white light photographic image was acquired, a fluorescent image was acquired using the following parameters: excitation filter = 675 nm, emission filter = 720 nm with f-stop set to 2 and an exposure time of 3 seconds, Field of View (FOV)=13.4 cm. *In vivo* and *ex vivo* image analysis was performed using Living Image Software (4.5.2 Version, PerkinElmer). For purposes of co-registering MRI with optical imaging, in vivo optical imaging was performed using Fluorescence Molecular Tomography (FMT) system (PerkinElmer). Following the animal preparation, the mice were transferred to the holding platform of the optical scanner and anesthesia was maintained with 0.5-2% isoflurane using an appropriate gas carrier nose cone installed in the scanner. Fluorescence Images were acquired using the following image acquisition parameters.

FMT excitation/emission wavelengths= 670/688nm, max Power of Class 3b laser=80mW, Cassette depth=15mm, ~100-120 excitation points in the scanfield. The collected fluorescence data was reconstructed using TrueQuant v3.0 software (PerkinElmer) for the quantification of three-dimensional fluorescence signal within an area /region of interest.

High resolution *ex vivo* optical imaging of kidneys was also performed using the Licor Odyssey Imager with an initial low resolution (337 μm) scout image on the lowest quality scan setting (~ 1- 1.5 min acquisition time) for the purpose of properly locating the kidneys in the scan field prior to acquiring the high resolution scan. The high resolution (21 μm) scan was acquired using highest quality scan setting with a total acquisition time approximately 8-10 minutes. The Image Studio version 5.2 software was used for image acquisition.

MRI was performed on a 9.4 Tesla horizontal bore system (Bruker Biospin, Billerica, MA). Prior to the start of the imaging session mice were physiologically monitored in the FMT cassette with ECG leads. A gradient echo tri-pilot sequence was used to generate a scout imaging. A 2D RARE sequence (TR/TE=1758/56 ms, FOV=78.85x78.85 mm, 256x256 pixel resolution) was followed with a 3D TurboRARE (TR/TE=200/27 ms, FOV=78.85x19.71x78.85 mm, 256x64x256 pixel resolution) and a 3D FLASH (TR/TE=16.1/5.4 ms, FOV=78.85x19.71x78.85 mm, 256x64x256 pixel resolution) sequence to generate 3D images of the mice.

Co-registration of FMT/MR images:

The spatial co-registration of the MRI and FMT images used a single software platform, VivoQuant™ (Version 2.5, InviCRO Inc.). VivoQuant is capable of handling multiple DICOM image inputs from different modalities and allows users to adjust the relative spatial position for each image input. FMT images were exported to 16-bit DICOM format by the TrueQuant 3.0 software. Multiple DICOM files and MRI raw data were imported into the VivoQuant data browser. The reorientation/registration tool was used to manually align multiple image datasets.

Confocal microscopy:

Blocks of tissue, previously frozen in liquid nitrogen and stored at -80 °C were placed in a cryostat and allowed to warm to chamber temperature of -13 °C. 6 µm sections were cut onto cold slides and warmed briefly to melt then returned to the cryostat until all sections were cut. Once all sections were cut the slides were removed from the cryostat, warmed until melted and placed in a humidified chamber for fixation and antibody incubations. Sections were fixed in 4% paraformaldehyde for 15 minutes then washed in PBS for an additional 15 minutes. The slides were then blocked for 15 minutes in 1% BSA. Slides were washed in PBS then incubated in the following mixture of primary antibodies diluted in 1% BSA for 1 hour at room temperature: 1 µg/ml rabbit anti-aquaporin 1 (EMD Millipore, Burlington, MA, Cat #Ab 2219) conjugated with Alexa 488 using Invitrogen's Zenon labeling kit (Invitrogen Thermo-Fisher, Waltham, MA, Cat# Z25302) and 1 µg/ml rabbit anti-megalin (Abcam, Cambridge, MA, Cat# 76969) labeled with Alexa 568 using the Zenon kit (Invitrogen, Cat# Z25306). Slides were washed for 15 minutes in PBS then mounted and cover slipped using ProLong Gold with DAPI (Invitrogen, Cat# P36935). Slides were viewed and imaged on a ZEISS LSM 780 confocal microscope.

Human Tissue Immunohistochemistry for Megalin Expression:

Human tissues used in these studies were approved at GSK plc. All donors provided written informed consent for use of their samples, and the collection and use of the samples received Institutional Review Board (or Ethics Committee) approval. A human kidney tumor tissue microarray (TMA) (Cat# Z7020054, Biochain Institute, Inc., Hayward, CA) was used for these studies; each core of the array had a diameter of 1.5 mm and the paraffin sections were 4µm thick. The TMA included neoplastic and non-neoplastic tissues (See Table 1). Most diagnoses were represented by cores from multiple patients and each patient's sample was provided in duplicate. All tumors were renal primaries, with no regional lymph node

metastasis and no distant metastasis. Immunohistochemistry of the paraffin section TMA was performed on an automated staining platform, Discovery Ultra (Ventana Medical Systems, Tucson, AZ). Briefly, the staining protocol included deparaffinization, high pH antigen retrieval (Ultra CC1, Cat# 950-224, Ventana Medical Systems, Tucson, AZ), protein block (SEA BLOCK blocking buffer, Cat# 37527, Thermo Fisher, Waltham, MA), incubation with either a rabbit anti-megalin antibody (Cat# A76969, Abcam, Cambridge, MA) or non-immune rabbit IgG (Cat# AB-105-C, R&D Systems, Minneapolis, MN) at 0.06µg/ml, detection with an alkaline phosphatase conjugated anti-rabbit IgG secondary antibody (UltraMap, Cat# 760-4314, Ventana Medical Systems, Tucson, AZ), antigen visualization (Discovery Red, Cat# 760-228, Ventana Medical Systems, Tucson, AZ), and hematoxylin nuclear counterstain (Hematoxylin II, Cat# 790-2208, Ventana Medical Systems, Tucson, AZ). Slides were air dried and then coverslipped with a synthetic mounting media. A TMA slide was stained for morphologic assessment using hematoxylin and eosin (H&E). Slides were scanned at 40X on a Hamamatsu Nanozoomer; images (Fig. 6) were extracted from the scans.

Separate studies were performed to evaluate Megalin and AQP1 co-expression in selected non-neoplastic and ccRCC tumors. For these studies, non-neoplastic renal tissue from a 67 year old female was obtained from NDRI; we acknowledge the use of this tissue procured by the National Disease Research Interchange (NDRI) with support from NIH grant U42OD11158). Additionally, ccRCC tissue from a 63 year old male was received from the MT Group (Van Nuys, CA). Both cases were fixed in 10% neutral buffered formalin and processed to paraffin block using standard histological technique; paraffin sections were made at 4µm and collected on glass slides. Immunohistochemistry was carried out on the staining platform described above, but a multiplex fluorescent approach was used to demonstrate expression and distribution of two separate proteins, megalin and AQP1. Briefly, the staining protocol included deparaffinization, high pH antigen retrieval (Ultra CC1, Cat# 950-224, Ventana Medical Systems, Tucson, AZ), protein block (SEA BLOCK blocking buffer, Cat# 37527, Thermo Fisher, Waltham, MA), incubation with either a cocktail that included rabbit anti-megalin antibody (Cat# A76969, Abcam, Cambridge, MA)

and mouse anti-AQP1 (Cat# A9566, Abcam, Cambridge, MA) or a cocktail of non-immune rabbit IgG (Cat# AB-105-C, R&D Systems, Minneapolis, MN) and non-immune mouse IgG2B (Cat# Ab18428, Abcam, Cambridge, MA); all antibodies and isotype negative controls were used at 0.25µg/ml. Secondary antibody detection was applied as a cocktail of goat anti-rabbit IgG conjugated to Alexa Fluor 594 (Cat# A-11037, Thermo Fisher) and goat anti-mouse IgG2B conjugated to Alexa Fluor 488 (Cat# A-21141, Thermo Fisher); both were applied at 6µg/ml. Slides were mounted using ProLong Gold with DAPI (Cat# P36935, Thermo Fisher) and viewed under fluorescent light using a Leica DM6000-B microscope; images were captured using Leica LAS X software (Leica Microsystems, Buffalo Grove, IL).

Statistical analysis:

All statistical analysis was perform using GraphPad Prism 6.0 software (GraphPad, San Diego, CA).

JPET Fast Forward. Published on April 1, 2019 as DOI: 10.1124/jpet.119.257022
This article has not been copyedited and formatted. The final version may differ from this version.

Results

Distribution of Renal Targeting KE peptide in control mice

Two KE peptides (11 aa and 16 aa) were conjugated to VivoTag 680 dye to enable *in vivo* NIR imaging and these peptide-dye conjugates were injected via an IV bolus (Fig.1A and 1B). In healthy control mice, optical imaging revealed that both GSK599A and GSK601A peptide-conjugated dyes preferentially localized to the kidney 4 hours post-injection (Fig.2A and 2B), while unconjugated VivoTag 680 was not detectable in kidney at this time. Serial *in vivo* optical imaging revealed that unconjugated VivoTag 680 dye renal signal was only observable 15 minutes post-injection in the kidney, but the signal was reduced to near-baseline levels by the 1 hour timepoint. In contrast, both GSK601A and GSK599A conjugates remained localized to the kidney at 15 min, 1 hour and 4 hour post-dose (Fig.2B) while moderately faster renal clearance was observed in GSK601A versus GSK599 treated animals.

Organs harvested for *ex vivo* optical imaging following the 4 hour post-dose timepoint revealed the unconjugated VivoTag 680 dye signal was present primarily in liver and kidney, but very low levels were also detectable in brain, heart, and spleen (Fig.2C and D). In marked contrast, strong signal was present predominantly in kidneys of GSK601A and GSK599A dosed animals, with far lower signal intensity present in liver, brain, heart, and spleen (Fig.2C and D). A modest, non-significant increase in optical signal was observed in GSK601A group compared to GSK599A group (Fig.2D). Divergent from the *in vivo* optimal imaging (Fig.2B), slightly more intense signal was observed for GSK601A compared to GSK599A with *ex vivo* imaging (Fig.2D). This may reflect the difference in optimal measurement including animal/organ positioning and potential light obstruction in the *in vivo* setting.

Sagittal sections of the kidneys were subsequently optically imaged (Fig.3A), revealing a low-intensity distribution of label throughout the kidney in sections from mice dosed with unconjugated VivoTag 680 dye (Fig.3A), whereas kidney sections from mice dosed with either GSK601A or GSK599A retained a high intensity signal that was located almost exclusively within the renal cortex (Fig.3A).

JPET Fast Forward. Published on April 1, 2019 as DOI: 10.1124/jpet.119.257022
This article has not been copyedited and formatted. The final version may differ from this version.

To confirm these observations at higher resolution, we examined kidney sections using confocal microscopy. In kidney sections from control mice dosed with VivoTag 680 dye (Fig.3B) there was no peptide signal (magenta, data not shown), while proximal tubule markers aquaporin 1 (AQ1) and megalin (Fig.3B) were colocalized in the cortex. In mice dosed with GSK599A, peptide-dye conjugate fluorescence (Fig.3B, magenta channel) localized exclusively within segments that stained positive for AQ1 (Fig.3B, green channel), and not within glomeruli, or distal tubules (arrows) (Fig.3B). These observations are consistent with a mechanism, within the proximal tubules, for selectively binding and retaining the GSK601A and GSK599A peptide-dye conjugates.

Furthermore, we performed high resolution MRI to co-register these anatomical images with our 3D optical FMT images in order to address the relative distribution and semi-quantitative signal localization with the kidney of the GSK599A and GSK601A peptides. Co-registration of FMT/MR images revealed highly specific kidney localization of both GSK601A and GSK599A 1 hour after dosing (Fig.4A-D). The quantitative analysis of the FMT-MRI to compare relative anatomical distribution of GSK599A and GSK601A 1 hour post-injection in cortical and non-cortical regions of the kidney showed a non-significant trend of increased medullary accumulation of the smaller GSK601A peptide compared to the cortex (Fig.4E). For GSK599A there was a more equivalent distribution between the medullary and cortex signals (Fig.4E). In contrast to the *ex vivo* images where the peptide signal was concentrated in cortex (Fig.3), *in vivo* FMT/MRI signal was more equivalent in the cortex and medulla, likely due to the filtration of dye into the medullary space *in vivo* and this signal being lost in the *ex vivo* setting.

Imaging of Renal Targeting KE peptide in JCK mice

After establishing the kidney localization of KE peptide-dye conjugates in control mice, we extended our study to a mouse model of polycystic kidney disease, the JCK mouse. This mouse strain displays consistent and rapid development of kidney cysts over several months, and has been extensively utilized to evaluate therapeutic agents. In our study, 14 week old JCK mice developed substantial and numerous cysts in the kidney (Fig.5C). In these JCK mice, we observed renal specific optical signal in

GSK599A and GSK601A dosed mice with no observable signal in the VivoTag 680 dye-treated mice (Fig.5A and 5B). High resolution *ex vivo* images in VivoTag 680 dye-treated mice showed generalized, non-specific distribution in the kidney whereas in GSK599A and GSK601A-treated mice there was a punctate, non-uniform signal specific to the renal cortex (Fig.5B). This pattern of peptide distribution was not observed in healthy mice (Fig.3). High resolution confocal microscopy in a representative mouse dosed with GSK599A revealed distended tubules/cysts (Fig.5D, cyst label) and complete overlap of AQ1 (green) and megalin (red) signal (Fig.5D). The confocal image confirmed the localization of the peptide in the proximal tubules (Fig.5D, magenta). Peptide-dye conjugate was localized in niches underneath the cyst lining, and completely co-localized with megalin and AQ1 immunoreactivity (Fig.5D). Importantly, the renal cysts were negative for AQ1 and megalin immunoreactivity and indicates that they did not bind and internalize peptide-dye conjugates (Fig.5D).

Megalin protein expression in human renal carcinoma

In order to expand our understanding of how renal pathology might affect megalin expression in human disease, we evaluated megalin protein expression in several types of renal cancer tissues (Fig.6). Review of the H&E stained tissues confirmed the normal and neoplastic diagnoses provided by the vendor. Normal human kidney tissue demonstrated specificity of megalin expression exclusively with structures consistent with proximal tubules (Fig.6 and Table 1). Multiplex immunofluorescent studies using megalin and AQP1 IHC demonstrated megalin expression is restricted to AQ1 positive proximal tubules of normal kidney tissue as well as neoplastic cells of ccRCC (Fig.6). Tissue specimens from a donor with a diagnosis of RCC demonstrated that 90% of the clear cell renal cell carcinoma (ccRCC) cases and 57% of the papillary renal cell carcinoma (pRCC) cases express megalin in the neoplastic cells (Fig.6 and Table 1). We did not detect megalin expression in any samples we evaluated from chromophobe renal cell carcinoma (chRCC) tissue (Fig.6A). Rabbit IgG isotype IHC controls did not exhibit specific staining (Fig.6A, right panels). We performed more detailed analysis with normal kidney and clear cell renal carcinoma (ccRCC) samples (Fig.6B). Significant overlapping expression pattern between APQ1 and megalin was observed in both

normal kidney sections and ccRCC tumors (Fig.6B). It is worth noting that the overall number of tumor cases we reviewed is small and analysis of additional tumor samples are needed to draw broader conclusions.

JPET Fast Forward. Published on April 1, 2019 as DOI: 10.1124/jpet.119.257022
This article has not been copyedited and formatted. The final version may differ from this version.

Discussion

The tissue specific delivery of therapeutic agents has been the focus of intensive investigations to enhance efficacy and minimize toxicity. Exploratory modalities have been evaluated to selectively target molecules into tissues such as the heart (Kanki et al., 2011; Zahid et al., 2018), tumors (Liu et al., 2017), and the liver (Mishra et al., 2013). Recently, studies have attempted to identify and characterize mechanisms that could selectively target therapeutic agents to the kidney, a concept that could expand the limited number of treatment options for chronic kidney disease by increasing the tolerability and/or limiting extra-renal toxicity of experimental therapeutics. Peptides with short lysine-glutamic acid $(KKEEE)_nK$ repeats, have been reported to efficaciously target small molecules to proximal tubule cells within the renal cortex of rats and multiple strains of mice (Wischnjow et al., 2016). In the current study, we extended these results and investigated whether these $(KKEEE)_nK$ peptides could selectively target the near-infrared dye VivoTag 680 to the kidney, if this targeting was consistent with megalin-dependent internalization by proximal tubule epithelial cells, and how this distribution would be altered in kidneys from mice with polycystic kidney disease phenotype.

We decided to perform optical imaging for these studies since the method does not require the use of radioactive labels unlike Positron Emission Tomography (PET). Using this methodology, we demonstrated that the VivoTag 680 dye signal heterogeneously distributes to the kidneys of healthy mice shortly after IV dosing (Fig.2), after which it is not detectable above the baseline optical signal at 1 hour post-dose. Post-mortem optical imaging revealed low intensity dye signals above background signals in all harvested organs (Fig.2), particularly liver and kidney, organs which receive a large fraction of cardiac output and play roles in clearance of xenobiotics. In marked contrast, both KKEEE-based peptide-dye conjugates, GSK599A and GSK601A, were detected almost exclusively within the kidney, consistent with selective renal targeting and retention of the KKEEE-based peptide conjugates. While determining the molecular receptor for these renal targeting peptides was beyond the scope of the present investigation, multiple lines of evidence support the hypothesis that megalin plays a key role for the uptake of these

peptide conjugates. Within the kidney, megalin is located on the apical surface of proximal tubule epithelial cells where it binds and internalizes filtered peptides and low molecular weight proteins. Indeed, both mice (Leheste et al., 1999) and humans (Storm et al., 2013) with mutations in the LRP2 gene that encodes megalin exhibit low molecular weight proteinuria. Thus, binding and reabsorption from ultrafiltrate of targeting peptides such as the ones we employed in the current study is consistent with the well-established physiological function of megalin.

In our experiments, both the 11 aa (GSK601A) and 16 aa (GSK599A) peptide conjugates selectively targeted the dye to the kidney cortex, while the 11 aa dye conjugate (GSK601A) had slightly more liver distribution, suggesting a longer sequence with charged amino acid residues could potentially be more precise in renal targeting. Janzer et al performed SAR analysis to determine the effects of peptide length, charge, and sequence on kidney targeting efficiency (Janzer et al., 2016). Additional SAR work may be required to optimize targeting efficiency while enhancing desirable pharmacokinetic (PK) properties in specific kidney disease models.

JCK mice have robust renal cyst formation due to a mutation in ciliary kinase NEK8 (Liu et al., 2002). Although the underlying genetic mutation is distinct from human ADPKD (PKD1 and PKD2 mutations), the mutation alters the expression and distribution of the mouse orthologs of these polycystin genes (Sohara et al., 2008) resulting in consistent and relatively rapid cyst formation/expansion and decline in renal function (Smith et al., 2006). In polycystic JCK mice, GSK599 similarly accumulated in the renal cortex as compared to healthy SKH1 control mice, and largely overlapped with megalin and AQ1-positive cells. In comparison to normal mice kidneys, distribution of KKEEE-conjugated dye within the cortex of JCK mice was limited and followed an irregular pattern (Fig.5). Interestingly, the dye localized to cells directly underneath the cyst lining epithelium, rather than the cyst lining itself. Confocal imaging revealed almost no staining for the proximal tubule marker AQ1 or megalin within the cortical cells lining the most distended and largest cysts, while the less distended regions retained expression of both AQ1 and megalin (green and red, respectively; Fig.5). We observed peptide-dye conjugate fluorescence only within these

JPET Fast Forward. Published on April 1, 2019 as DOI: 10.1124/jpet.119.257022
This article has not been copyedited and formatted. The final version may differ from this version.

latter regions, demonstrating that the cyst-lining cells that have potentially ceased expressing AQ1 and megalin have also lost their ability to bind and/or retain peptide-dye conjugates. Consistent with our findings, the loss of megalin expression in mature cysts was also reported in *pkd1* knockout mice (Ahrabi et al., 2010). In addition, a rat model of ADPKD showed the loss of endocytosis capacity was likely associated with reduced megalin expression (Obermuller et al., 2001). In humans, there has been debate as to the specific cellular origin of cysts. Studies by Grantham et al involving the lineage of human cyst cells, suggested that cyst epithelium is derived from proximal tubules as well as from collecting duct, glomerular visceral tissues and other undetermined, none-typical tubule origin (Grantham et al., 1987).

While our data suggest the KE peptide does not directly localize to cyst lining, targeting megalin-positive proximal tubular cells with this approach may still be appropriate for ADPKD due to the proximity of the megalin-positive cells to the cyst lining itself and underlying stromal tissues. Depending upon the properties of the molecule, extent of target engagement needed for efficacy, and the renal microenvironment, this targeted approach could enable the enrichment of therapeutic agents specifically in affected cells or niches within the kidney and minimize unwanted effects on other unaffected tissue or organs. Our data validates the kidney cortex-specific distribution of these peptide-dye conjugates and lays the foundation for additional investigative work into other kidney diseases, particularly those involving the proximal tubules such as renal tubular acidosis, Dent's disease, and amino acid transport diseases (Nakhoul and Batuman, 2011).

RCC is a group of malignancies arising from the epithelium of the renal tubules and represents over 90% of renal malignancies (Ebler et al., 2004). Included in this group are ccRCC, pRCC, and chRCC with ccRCC accounting for about 70% of the cases reviewed (Jennette et al., 2015). It has been demonstrated ultrastructurally that ccRCC arises from epithelial cell of the renal convoluted tubule and that AQ1 expression in ccRCC and pRCC are significantly greater than in chRCC, oncoytomas, and collecting duct tumors (Oberling et al., 1960; Maunsbach et al., 1997; Huang et al., 2009). Our study represents the first IHC report of megalin expression in human ccRCC and pRCC. Our results, albeit with a small collection

of RCC cases, indicate a significant portion of ccRCC and pRCC cases are megalin positive and warrant additional studies. The targeted delivery strategy described here could potentially be applicable to RCC tumor treatment.

The dependency of this peptide-based delivery mechanism on the presence of megalin prompts some intriguing questions regarding the optimal design of targeting agents and the most suitable disease indications. Megalin mediates reuptake of glomerular filtrated protein and small peptides to maintain protein homeostasis. Disruption of this gene is associated with low molecular weight proteinuria and progression to ESRD (Eshbach and Weisz, 2017). This mechanism dictates that the putative kidney targeting agent will likely be a small molecule rather than larger proteins such as antibodies conjugated to the targeting peptide that is resistant to proteolytic environments in circulation and in filtered urine, and that it be taken up via endocytosis into targeted megalin-positive proximal tubular cells. The drug will then be decoupled or released from the conjugate and migrate to its true target site for therapeutic action inside the cell. In this regard, targeting the therapeutic small molecule to the kidney is merely the first step. Accumulation of drug in the proper cell types in sufficient concentrations, enabling the release of the therapeutic moiety, and achieving biological efficacy would all constitute additional challenges for a successful targeted, kidney-specific delivery. Additionally, whether this megalin-based targeting approach will be effective in patients with existing proteinuria, where filtered proteins may compete with targeting vectors for megalin binding, such as those in later stages of chronic kidney disease or diabetic kidney disease, is another uncertainty that warrants further investigation.

In summary, our results represent the first imaging study of a peptide-based renal targeting approach in a mouse model of human ADPKD disease. Highly enriched renal-specific targeting was achieved, and peptide-dye conjugates were localized in megalin-positive renal proximal tubular cells underneath the cyst lining. As such, this may represent an attractive strategy to target therapeutic agents to treat ADPKD and other tubular renal diseases. Additionally, megalin positive ccRCC may also be a suitable disease for this modality.

Acknowledgement

We wish to thank Robert Willette and Luke Devey of GlaxoSmithKline Plc for their support of this project.

Authorship contributions

Participated in research design: Hu, Lee, Jucker, McAlexander, Lenhard, Virtue.

Conducted experiments: Lenhard, Fieles, Skedzielewski, Rambo, Trinh, Geske.

Contributed new reagents or analytic tools: Lenhard, Fieles, Cheng, Ilobet, Nadin, Skedzielewski, Fieles, Geske, Klein.

Performed data analysis: Lenhard, McAlexander, Fieles, Virtue, Hong, Geske, Klein, Jucker, Trinh, Virtue, Skedzielewski, Rambo.

Wrote or contributed to the writing of the manuscript: Hu, Jucker, McAlexander, Lenhard, Virtue.

References:

Ahrabi AK, Jouret F, Marbaix E, Delporte C, Horie S, Mulroy S, Boulter C, Sandford R and Devuyst O (2010) Glomerular and proximal tubule cysts as early manifestations of Pkd1 deletion. *Nephrol Dial Transplant* **25**:1067-1078.

Chapman AB, Devuyst O, Eckardt KU, Gansevoort RT, Harris T, Horie S, Kasiske BL, Odland D, Pei Y, Perrone RD, Pirson Y, Schrier RW, Torra R, Torres VE, Watnick T, Wheeler DC and Conference P (2015) Autosomal-dominant polycystic kidney disease (ADPKD): executive summary from a Kidney Disease: Improving Global Outcomes (KDIGO) Controversies Conference. *Kidney Int* **88**:17-27.

Christensen EI and Birn H (2002) Megalin and cubilin: multifunctional endocytic receptors. *Nat Rev Mol Cell Biol* **3**:256-266.

De S, Kuwahara S and Saito A (2014) The endocytic receptor megalin and its associated proteins in proximal tubule epithelial cells. *Membranes (Basel)* **4**:333-355.

Ebler JN, Sauter G, Epstein G and Sesterhenn IA (2004) *World Health Organization Classification of Tumours. Pathology and Genetics of Tumours of the Urinary System and Male Genital Organs. .* IARC Press, Lyon France.

Eshbach ML and Weisz OA (2017) Receptor-Mediated Endocytosis in the Proximal Tubule. *Annu Rev Physiol* **79**:425-448.

Grantham JJ, Geiser JL and Evan AP (1987) Cyst formation and growth in autosomal dominant polycystic kidney disease. *Kidney Int* **31**:1145-1152.

Huang Y, Murakami T, Sano F, Kondo K, Nakaigawa N, Kishida T, Kubota Y, Nagashima Y and Yao M (2009) Expression of aquaporin 1 in primary renal tumors: a prognostic indicator for clear-cell renal cell carcinoma. *Eur Urol* **56**:690-698.

Janzer M, Larbig G, Kubelbeck A, Wischnjow A, Haberkorn U and Mier W (2016) Drug Conjugation Affects Pharmacokinetics and Specificity of Kidney-Targeted Peptide Carriers. *Bioconjug Chem*.

Jennette JC, D'Agati VD, Olson JL and Silva FG (2015) *Heptinstall's Pathology of the Kidney, 7th ed.* Wolters Kluwer, Philadelphia, USA.

Kanki S, Jaalouk DE, Lee S, Yu AY, Gannon J and Lee RT (2011) Identification of targeting peptides for ischemic myocardium by in vivo phage display. *J Mol Cell Cardiol* **50**:841-848.

Leheste JR, Rolinski B, Vorum H, Hilpert J, Nykjaer A, Jacobsen C, Aucouturier P, Moskaug JO, Otto A, Christensen EI and Willnow TE (1999) Megalin knockout mice as an animal model of low molecular weight proteinuria. *Am J Pathol* **155**:1361-1370.

Liu S, Lu W, Obara T, Kuida S, Lehoczky J, Dewar K, Drummond IA and Beier DR (2002) A defect in a novel Nek-family kinase causes cystic kidney disease in the mouse and in zebrafish. *Development* **129**:5839-5846.

Liu X, Lin P, Perrett I, Lin J, Liao YP, Chang CH, Jiang J, Wu N, Donahue T, Wainberg Z, Nel AE and Meng H (2017) Tumor-penetrating peptide enhances transcytosis of silicasome-based chemotherapy for pancreatic cancer. *J Clin Invest* **127**:2007-2018.

Maunsbach AB, Marples D, Chin E, Ning G, Bondy C, Agre P and Nielsen S (1997) Aquaporin-1 water channel expression in human kidney. *J Am Soc Nephrol* **8**:1-14.

Mishra N, Yadav NP, Rai VK, Sinha P, Yadav KS, Jain S and Arora S (2013) Efficient hepatic delivery of drugs: novel strategies and their significance. *Biomed Res Int* **2013**:382184, PMID: 24286077.

Muller RU and Benzing T (2018) Management of autosomal-dominant polycystic kidney disease-state-of-the-art. *Clin Kidney J* **11**:i2-i13.

Nakhoul N and Batuman V (2011) Role of proximal tubules in the pathogenesis of kidney disease. *Contrib Nephrol* **169**:37-50.

Oberling C, Riviere M and Haguenau F (1960) Ultrastructure of the clear cells in renal carcinomas and its importance for the demonstration of their renal origin. *Nature* **186**:402-403.

Obermuller N, Kranzlin B, Blum WF, Gretz N and Witzgall R (2001) An endocytosis defect as a possible cause of proteinuria in polycystic kidney disease. *Am J Physiol Renal Physiol* **280**:F244-253.

Smith LA, Bukanov NO, Husson H, Russo RJ, Barry TC, Taylor AL, Beier DR and Ibraghimov-Beskrovnaya O (2006) Development of polycystic kidney disease in juvenile cystic kidney mice: insights into pathogenesis, ciliary abnormalities, and common features with human disease. *J Am Soc Nephrol* **17**:2821-2831.

Sohara E, Luo Y, Zhang J, Manning DK, Beier DR and Zhou J (2008) Nek8 regulates the expression and localization of polycystin-1 and polycystin-2. *J Am Soc Nephrol* **19**:469-476.

Storm T, Tranebjaerg L, Frykholm C, Birn H, Verroust PJ, Neveus T, Sundelin B, Hertz JM, Holmstrom G, Ericson K, Christensen EI and Nielsen R (2013) Renal phenotypic investigations of megalin-deficient patients: novel insights into tubular proteinuria and albumin filtration. *Nephrol Dial Transplant* **28**:585-591.

Weimbs T, Shillingford JM, Torres J, Kruger SL and Bourgeois BC (2018) Emerging targeted strategies for the treatment of autosomal dominant polycystic kidney disease. *Clin Kidney J* **11**:i27-i38.

Wischnjow A, Sarko D, Janzer M, Kaufman C, Beijer B, Brings S, Haberkorn U, Larbig G, Kubelbeck A and Mier W (2016) Renal Targeting: Peptide-Based Drug Delivery to Proximal Tubule Cells. *Bioconjug Chem* **27**:1050-1057.

Zahid M, Feldman KS, Garcia-Borrero G, Feinstein TN, Pogodzinski N, Xu X, Yurko R, Czachowski M, Wu YL, Mason NS and Lo CW (2018) Cardiac Targeting Peptide, a Novel Cardiac Vector: Studies in Bio-Distribution, Imaging Application, and Mechanism of Transduction. *Biomolecules* **8**:PMID: 30441852

JPET Fast Forward. Published on April 1, 2019 as DOI: 10.1124/jpet.119.257022
This article has not been copyedited and formatted. The final version may differ from this version.

Legends for Figures

Figure 1. **Optical imaging study design and structures for VivoTag-680 Dye, GSK599A, and GSK601A**. (A) VivoTag 680 Control Dye, GSK601A $(KKEEE)_2K$, and GSK599A $(KKEEE)_3K$ peptide-dye conjugate structures. (B) *In vivo* optical imaging study design denoting imaging timepoints following IV injection.

Figure 2. *In vivo* and *ex vivo* optical imaging in control mice. (A) Representative VivoTag-680 Dye, GSK599A, and GSK601A *in vivo* optical images 4 hours post-injection. (B) Renal optical signal at 15 minutes, 1 hour, and 4 hours post-injection. n=4-6; error bars indicate mean ± SEM. ****indicates $p<0.0001$ (one-way ANOVA with a multiple comparison test). (C) Representative *ex vivo* images of brain, heart, liver, spleen, and kidneys in VivoTag 680 Dye, GSK599A, and GSK601A-treated mice. (D) *Ex vivo* organ optical signals in VivoTag-680 Dye versus GSK599A and GSK601-treated groups.

Figure 3. High resolution *ex vivo* optical imaging of kidney from VivoTag 680 Dye, GSK599A, and GSK601A treated mice and confocal immunohistochemical microscopy. (A) Representative high resolution *ex vivo* optical image of VivoTag 680 dye, GSK599A, and GSK601A mouse kidneys. mouse kidneys. Optical cortical signal was saturated in GSK599A and GSK601A images. (B) Representative confocal images of the cortex of a kidney treated with VivoTag 680 dye (upper panels) stained for proximal tubules marker AQ1 (green), Megalin (red), and DAPI (blue). The lower panels are representative confocal images of the kidney cortex of mice treated with GSK599A and stained with AQ1 (green), peptide (magenta), and DAPI (blue). Other structures including glomeruli (G) as well as distal and collecting tubules (arrows) are labelled.

Figure 4 – Co-registration of VivoTag 680 Dye signaling with FMT/MRI analysis

(A/B) Co-registered MRI and Fluorescence Molecular Tomography (FMT) coronal and sagittal images of a representative control mouse 1 hour following injection of GSK599A. (C/D) Co-registered MRI and FMT coronal and sagittal images of a representative animal 1 hour following injection of GSK601A. E) Quantitative analysis of cortical and medullary signal. The variations in optical signals in cortex and medulla in both treated groups are not statistically significant ($p>0.05$), (non-parametric, paired t-test). n=3-6; error bars indicate mean ± SEM.

Figure 5. ***In vivo* and *ex vivo* optical imaging in JCK Mouse**. (A) *In vivo* images of 14 week old JCK mice showing accumulation of GSK599A and GSK601A in the kidney at 1 hour post-dose. Only one kidney was observable in the GSK599A group due to positioning of the mouse in the optical scanner. (B) *Ex vivo* images of 14 week old JCK kidneys (white is saturated signal). (C) H&E images of kidney sections from normal and 14 week old JCK mice. Black bar is 1mm in scale. (D) 4 confocal microscopy images of cyst areas with AQ1 (green), DAPI (blue), Megalin (red), and GSK599A (magenta) stain in 14 week old JCK mouse kidney dosed with GSK599A.

Figure 6. Megalin Expression in Normal Human Kidney and Renal Tumors

(A) Megalin expression in normal kidney and tumors including ccRCC, pRCC, and chRCC (Scale bar = 100µm). H&E stained TMA cores (left panels) are included to demonstrate expected normal or neoplastic morphology. Middle panels are IHC stained cores for megalin; cells expressing megalin are red with blue nuclei. Right panels are matched isotype negative control sections and are absent of any non-specific staining showing only the blue nuclear counterstain. G = glomerulus, PT = Proximal Tubule, DT = Distal Tubule. Arrowheads demonstrate areas of neoplastic cells. ccRCC: clear cell renal carcinoma; pRCC: papillary renal carcinoma; chRCC: chromophobe renal carcinoma. (B) Normal kidney (upper panels) and ccRCC kidney (lower panels) sections stained for megalin (red), and DAPI (blue). (Scale bar = 100µm).

Table 1 Legend:

Summary results for megalin expression in neoplastic and non-tumor tissue. ccRCC: clear cell renal carcinoma; pRCC: papillary renal carcinoma; chRCC: chromophobe renal carcinoma.

JPET Fast Forward. Published on April 1, 2019 as DOI: 10.1124/jpet.119.257022
This article has not been copyedited and formatted. The final version may differ from this version.

Table 1: Megalin protein expression in human renal tumors

Immunohistochemical Evaluation of Megalin Expression			
Diagnosis	**# cases**	**Megalin +/ve**	**% Positive**
Non-cancerous kidney biopsy	**4**	**4**	**100%**
Clear Cell Carcinoma (ccRCC)	**20**	**18**	**90%**
Papillary Renal Carcinoma (pRCC)	**7**	**4**	**57%**
Transitional Cell Carcinoma	**3**	**0**	**0%**
Chromophobe Renal Cell Carcinoma (chRCC)	**3**	**0**	**0%**

JPET Fast Forward. Published on April 1, 2019 as DOI: 10.1124/jpet.119.257022
This article has not been copyedited and formatted. The final version may differ from this version.

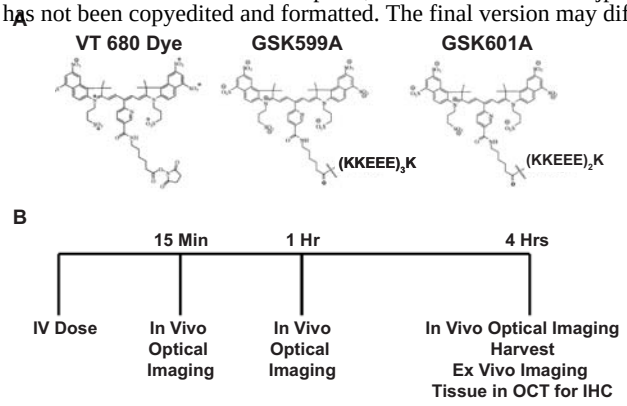

Figure 1

JPET Fast Forward. Published on April 1, 2019 as DOI: 10.1124/jpet.119.257022
This article has not been copyedited and formatted. The final version may differ from this version.

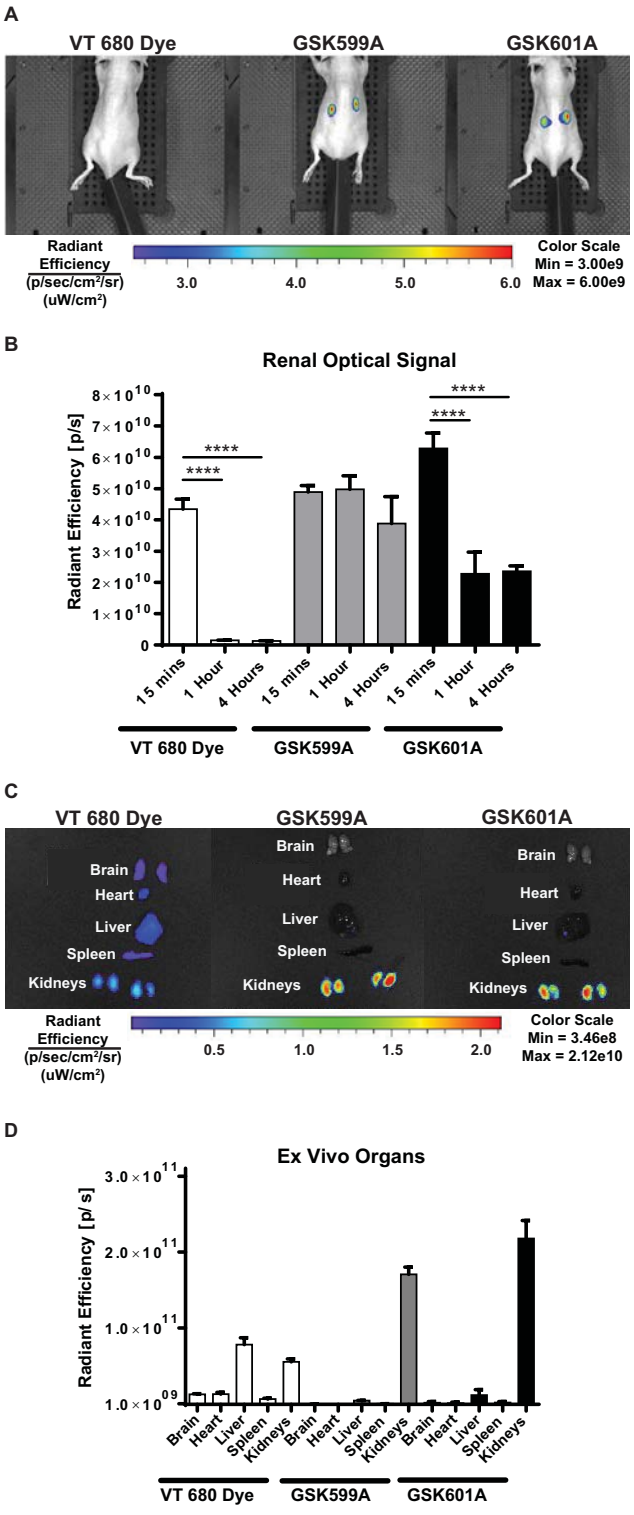

Figure 2

JPET Fast Forward. Published on April 1, 2019 as DOI: 10.1124/jpet.119.257022
This article has not been copyedited and formatted. The final version may differ from this version.

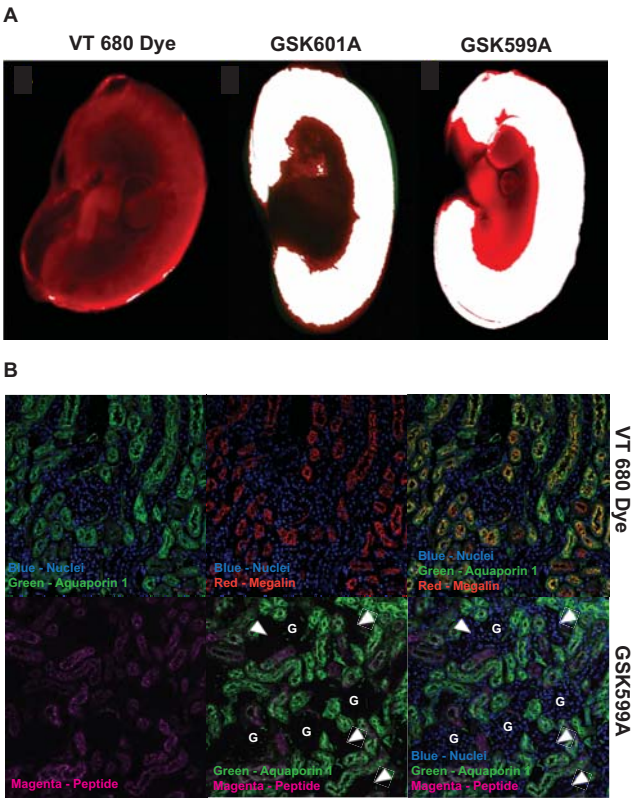

Figure 3

JPET Fast Forward. Published on April 1, 2019 as DOI: 10.1124/jpet.119.257022
This article has not been copyedited and formatted. The final version may differ from this version.

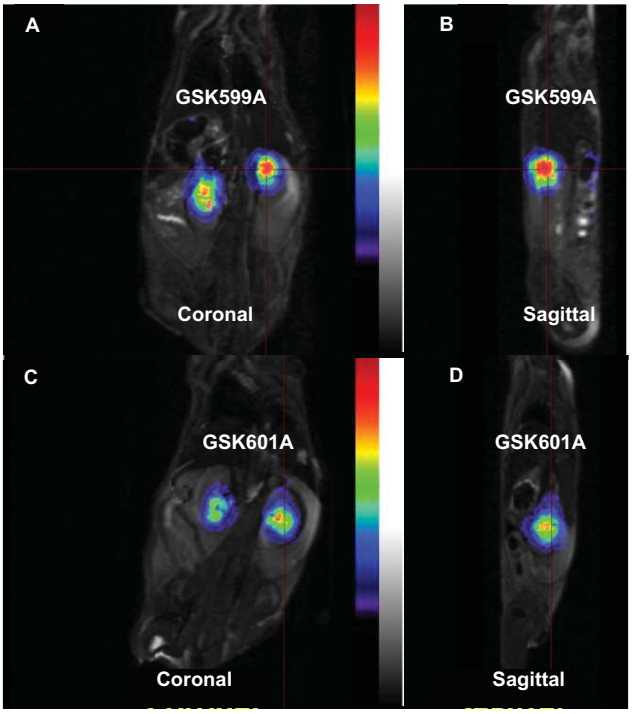

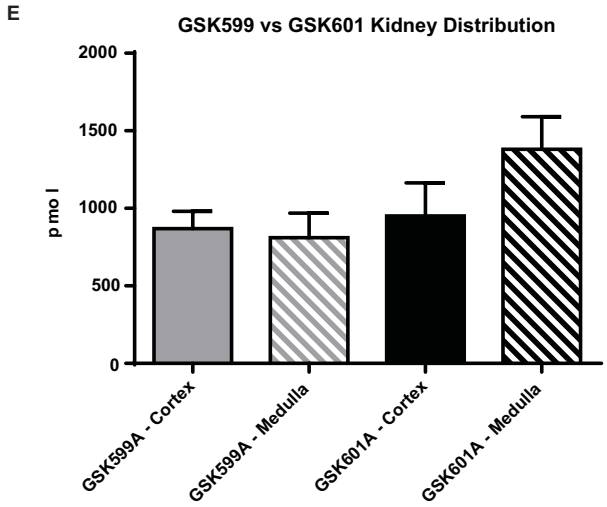

Figure 4

JPET Fast Forward. Published on April 1, 2019 as DOI: 10.1124/jpet.119.257022
This article has not been copyedited and formatted. The final version may differ from this version.

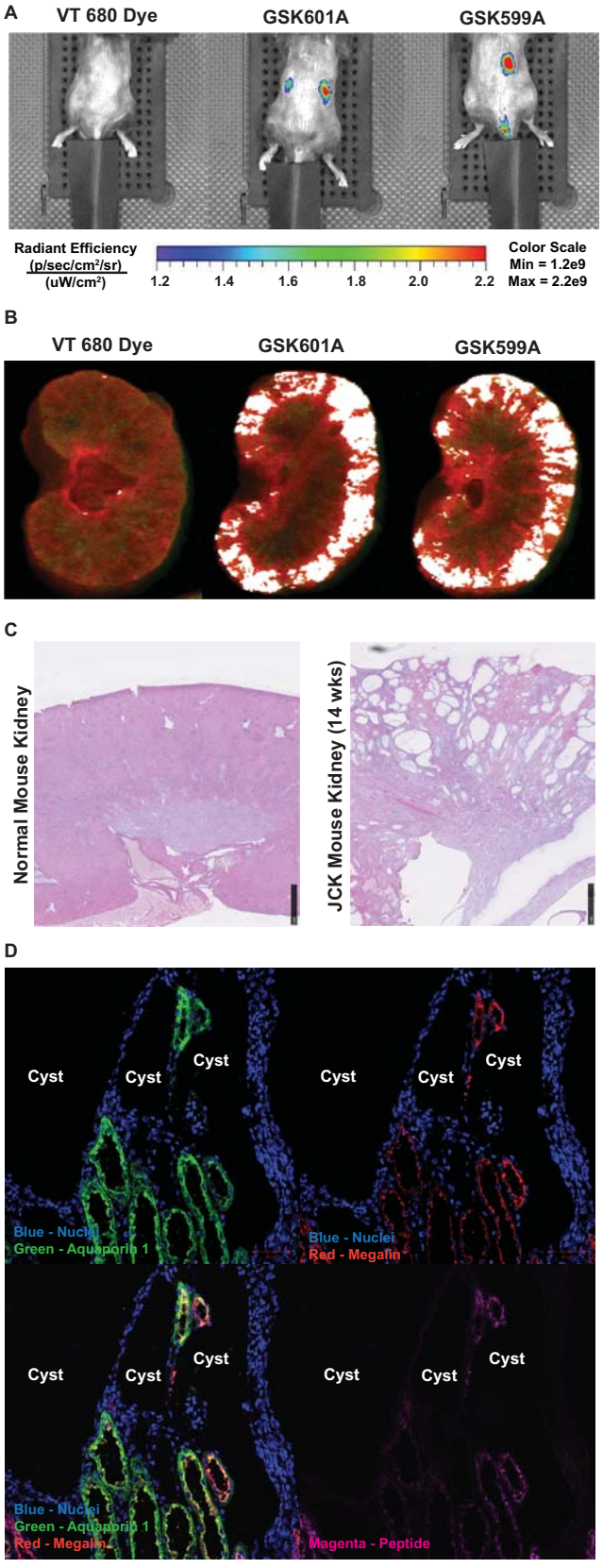

Figure 5

JPET Fast Forward. Published on April 1, 2019 as DOI: 10.1124/jpet.119.257022
This article has not been copyedited and formatted. The final version may differ from this version.

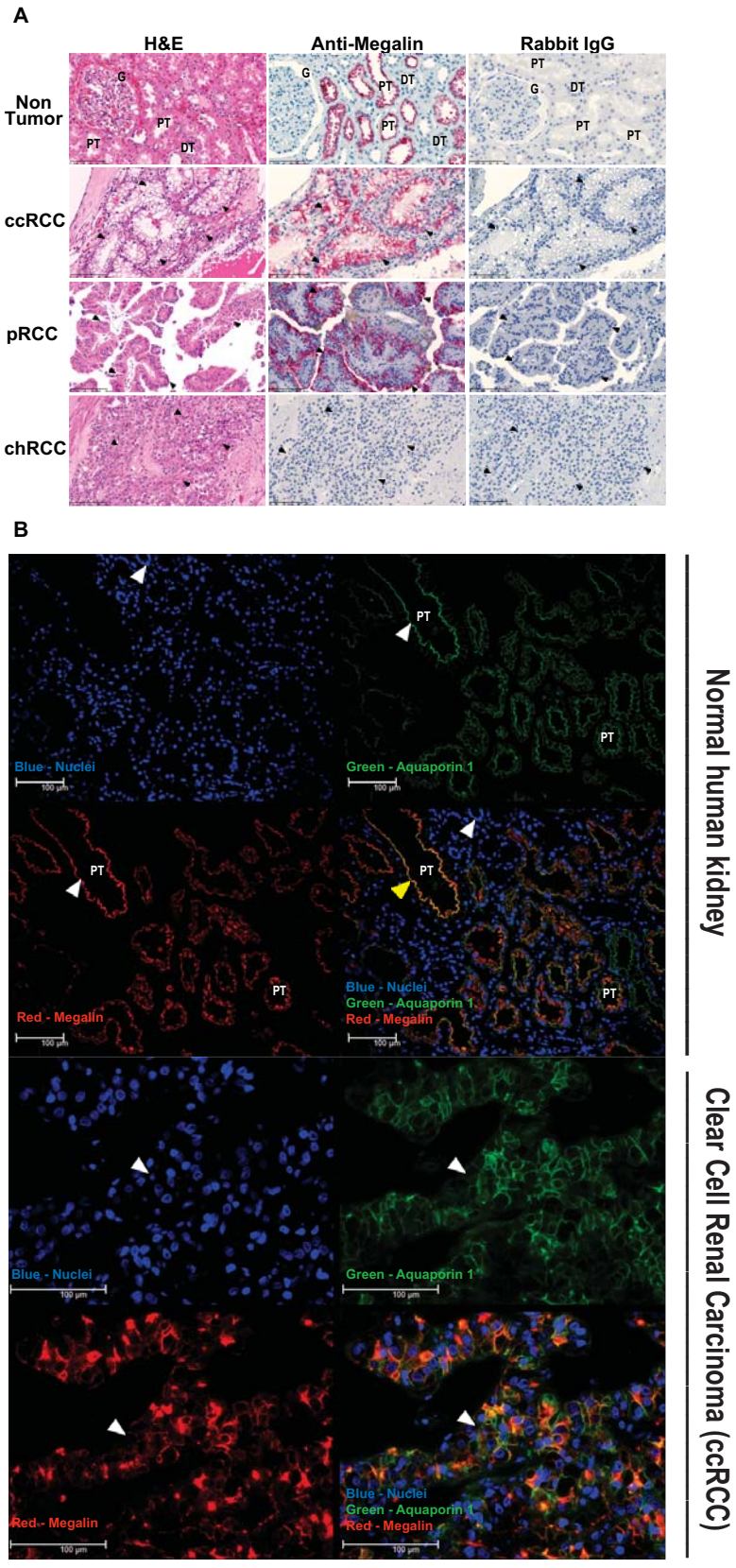

Figure 6